Available online at www.sciencedirect.com
ScienceDirect
Journal of the European Ceramic Society 31 (2011) 2793–2807
www.elsevier.com/locate/jeurceramsoc

CO_2 laser underwater machining of deep cavities in alumina

Yinzhou Yan [a,b], Lin Li [a,*], Kursad Sezer [a], Wei Wang [a], David Whitehead [a], Lingfei Ji [b], Yong Bao [b], Yijian Jiang [b]

[a] *Laser Processing Research Centre, School of Mechanical, Aerospace and Civil Engineering, The University of Manchester, Manchester M13 9PL, UK*
[b] *Institute of Laser Engineering, Beijing University of Technology, Beijing 100124, PR China*

Received 22 January 2011; received in revised form 7 June 2011; accepted 24 June 2011
Available online 15 August 2011

Abstract

A method for crack-free machining of deep cavity in alumina is demonstrated using a low-cost CO_2 continuous wave (CW) laser. CO_2 laser underwater machining has been found to result in reducing substrate defects such as recast layer, dross, cracking and heat damages that are typically found in machining in air. Finite Element (FE) modelling technique and Smooth Particle Hydrodynamic (SPH) modelling technique were employed to understand the effect of water on crack resistance and debris removal during underwater machining. Also the microstructures of machined region were demonstrated to reveal different heating and cooling processes during laser machining in water and in air. The experimental results indicated that the machined kerf width was strongly affected by the water layer thickness, whereas the kerf depth was controlled by both the laser pass number and water layer thickness. The optimal average machining rate was up to 2.95 mm^3/min at a 60 W laser power.

Keywords: Al_2O_3; Milling; Defects; Structural integrity; Laser machining; Finite element modelling (FEM); Smooth particle hydrodynamic (SPH)

1. Introduction

Alumina is one of the most used structural ceramics in a variety of applications ranging from microelectronics to prosthetics due to its desirable properties, such as high hardness, low chemical reactivity, low mass density, low thermal and electrical conductivity and ultra-fine finishing capability.[1] However, these applications require fast processing, tight dimensional tolerance and excellent surface finish. Therefore, processing and manufacturing of alumina with high accuracy become very important. Conventional ceramic machining techniques use diamond grinding to remove the material, which often leads to fracture, tool failure, low surface integrity, high energy consumption, and tool wear.[1,2] Furthermore, the closed and complex cavity machining poses more challenges to traditional machining techniques. As a result of the lacking of techniques for machining high precision and complex shapes for ceramics, laser beam machining techniques have been developed due to the unique advantages of the laser processes, such as high energy density, non-contact machining, high feed rate, high precision, and small heat-affected zone (HAZ).

Although CO_2 lasers and Nd:YAG lasers have been widely used for machining of ceramics, defects such as cracking and recast layers often occurred due to rapid cooling, high thermal gradients and brittleness of the materials. Especially, the continuous wave (CW) lasers were rarely used directly for machining ceramics at room temperatures in air without forced cooling (i.e. assist-gas) due to high stress developments caused by the serious heat generation in ceramics. Nisar et al. studied the effect of continuous and pulsed laser beam modes on thermal-stress developments in diode laser controlled fracture machining of glass. They found that the short pulse lengths can reduce thermal-stresses and arrest the crack propagation.[3] Zeng et al. reported laser carving of 3D structures in alumina substrates using a short pulsed CO_2 laser, by which a 15 mm × 14.27 mm × 2.5 mm cavity was obtained within 50 min. They found the process quality was mainly dependent on the parameters such as pulse repetition rate, scanning speed, pulse energy, interval of scanning lines and slicing thickness.[4] Hand et al. examined the parameters for a nanosecond pulsed (60 ns) Nd:YAG laser crack-free machining of yttria-stabilized tetragonal zirconia polycrstal (Y-TZP) ceramics. They found that the combination of processing

* Corresponding author. Tel.: +44 1613063814.
E-mail address: Lin.li@manchester.ac.uk (L. Li).

0955-2219/$ – see front matter © 2011 Elsevier Ltd. All rights reserved.
doi:10.1016/j.jeurceramsoc.2011.06.015

variables (at an average power of 11.3 W, a repetition rate of 30 kHz and a scan speed of 50 mm/s) provides the optimum material removal rate up to ~2 mm^3/min for machining Y-TZP ceramics. Additionally, it was found that the pulse overlap has a significant influence on the process efficiency and hence the combination of scan speed and repetition rate should be carefully considered. Their experimental results showed that too much pulse overlap or insufficient pulse overlap could create low quality machined surfaces.[5] In order to improve the process efficiency of nanosecond pulsed laser machining, Hand et al. presented a method of nanosecond-laser post-processing of millisecond-laser machined Y-TZP surfaces. A millisecond laser (0.3–5 ms) system was first used to provide a "rough machining" process with a high-speed material removal due to the high average power available, in which the material removal rate was up to 2.5 mm^3/s without significant cracking. However, the quality of the finished surface is limited by recast layer formation and heat-affected zones, in particular surface micro-cracks. A nanosecond laser (50–100 ns) system was then used to finish the "fine machining" process in a relatively short time.[6] The nanosecond laser post-processing of millisecond laser machined surface used two different sets of parameters to combine an optimal material removal rate at 15 kHz for the removal of the recast layers with a lower thermal impact machining at 60 kHz to further reduce the extent of cracking.[7] However, the pulsed laser ablation needed a high power source and machined surface had a relatively high roughness due to the inherent profile of overlapping of the pulses. Moreover, the dual-laser processing technique would be costly for industrial applications. Tsai et al. developed a fracture-machining element technique for the milling of closed cavities in alumina substrates,[8] which was based on the controlled fracture machining technique.[9] It employed crack propagation to achieve material removal and attained a high material removal rate 0.15 mm^3/s with less material melting during process. However, the complicated system consisting of dual lasers (a CO_2 laser and an Nd:YAG laser) was inevitable. Most importantly, the process quality did not satisfy the industrial requirements. A post-process for smoothing the surface was essential before final uses. For a high process quality, picosecond and femtosecond lasers have been applied in previous research, but the material removal rates were very low (2.2 mm^3/min and 0.054 mm^3/min, respectively) and the expensive systems are only suitable for micro-machining.[10,11]

Laser-assisted machining (LAM) is another alternative technique for machining of ceramics. During LAM, the workpiece is heated intensely and locally by a laser beam, and then machined with a conventional cutting tool.[12] Due to the advantage of lowered hardness and brittleness of the material at elevated temperatures, LAM can achieve lower cutting forces, reduced tool wear, higher material removal rates, and better surface quality for various advanced ceramics, such as alumina,[13] silicon nitride,[14] mullite,[15] and magnesia-partially stabilized zirconia.[16] LAM includes laser-assisted turning and laser-assisted milling.[17] Laser-assisted milling has been successfully performed for milling of silicon nitride[18–21] and alumina ceramics.[13] Unfortunately, effective cooling of the cutting tool, optimisation of the machining process and flexible control of the laser source to achieve complex pattern machining are the challenging tasks for laser-assisted milling,[17] which limit LAM for further industrial applications. Until now, laser beam machining is still considered as a desirable technique for machining of hard-to-machine materials due to its unique advantages, such as flexible machining process, compact system structure, controllable process parameters, and high material removal rate.

The main challenge for laser machining in air condition is the heat accumulation and molten material resolidification onto the machined surfaces, which cause serious HAZs and crack initiation. In 1988, Morita et al. first reported the pulsed YAG laser drilling of ceramics in water.[22] They found that the recast layer and cracks that were always formed during machining in air could be avoided in underwater machining. Kruusing further reviewed the advantages and disadvantages of water-assisted laser processing and concluded that the underwater machining techniques can be successfully applied to etching, cutting, surface cleaning, and shock processing.[23,24] In previous studies, the Nd:YAG laser emitted at 1.06 μm was considered as an ideal laser for underwater machining due to the low optical energy absorption of water with respect to this wavelength.[25,26] On the other hand alumina and glass also have a low absorption for a YAG laser compared with a CO_2 laser. Therefore, CO_2 laser underwater machining was developed. The mechanism of CO_2 laser underwater machining is different from that with a YAG laser due to the high absorption of water for the 10.6 μm wavelength CO_2 laser. During CO_2 laser underwater machining, a proportion of the laser energy vaporises the water and forms a conical keyhole in water allowing the laser beam to reach the workpiece. Black et al. found that the thermal load during CO_2 laser underwater cutting of ceramic tile was reduced by the intensive cooling effect of water.[27] Chung et al. employed a CO_2 laser with galvanometer mirrors to achieve crack-free drilling and cutting of Pyrex glass, where the defects of bugle, debris, cracks and scorch often occurred during laser machining in air were eliminated in underwater machining.[28,29] Tsai et al. performed a wide range of experiments on laser drilling and trepanning of thin glass and alumina substrates in air and in water. They found that the underwater drilling quality is much better than that in air. Underwater drilling could prevent the micro-cracking and reduce the HAZ.[30]

Although many investigations focused on the underwater drilling and cutting of thin ceramic or glass substrates, few studies pay attention to the cavity machining for alumina in water, especially machining of mm-deep cavity. Many studies discussed the mechanism of underwater laser processing, but the benefits of the process have not been entirely revealed. Moreover, the machining parameters for CO_2 laser underwater milling of deep cavity in alumina have not been studied before.

In this work, underwater machining of deep cavities in alumina ceramic using a low-cost CO_2 continuous wave (CW) laser was studied. Finite element modelling technique was employed to study the temperature and resulting stress distributions during laser machining in air and in water, in order to understand the mechanism of underwater crack-free machining. The crack formation during machining in air was also predicted based on the FE simulated result and validated via experiments. The effect

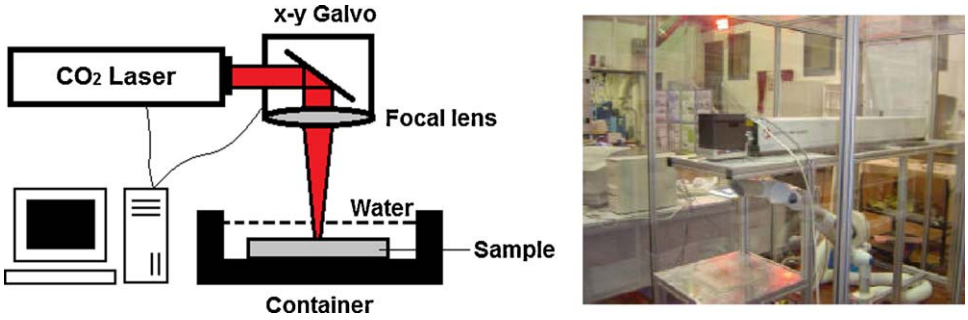

Fig. 1. Schematic diagram of experimental setup for underwater machining of alumina. The sample was submerged into the water at room temperature.

of fluid dynamics of water on debris removal was discussed to explain the process of material removal causing smooth side wall surfaces during underwater machining, with the aid of smooth particle hydrodynamic (SPH) technique, which was applied for the first time to study laser machining of ceramics. Then the effects of water layer thickness and scanning pass number on process quality and material removal rate were investigated. Finally, some mm-deep polygon cavities machined underwater with the optimised process parameters were demonstrated.

2. Experimental procedure

Fig. 1 shows the experimental setup of the CO_2 laser underwater machining system, which includes a Spectron CO_2 CW laser ($M^2 < 1.2$) with a maximum laser power of 100 W, an x–y galvanometer beam scanner, a focal lens with a focal length of 300 mm and a sample container with water. The specimen is 95% alumina ceramic with a thickness of 8 mm. The major thermal and mechanical properties of the material are listed in Table 1. The sample was submerged in water at the room temperature. The focused laser beam with selected process parameters was delivered onto the workpiece through the water layer. The focal plane position was set on the surface of the workpiece giving a spot size of 0.5 mm. A computer aided design program was used to set the scanning pattern and process parameters.

In this work, the effects of water layer thickness and scanning pass number were investigated to understand the mechanism of underwater machining. It was found that a 2 mm stationary water layer was necessary to wet the alumina surface during machining. The laser machining in air was also performed as a reference sample for comparison. Two machining modes were used in this work. The 30 mm straight lines by multi-pass scanning were performed (Fig. 2(a)) to study the machining depth and width at different water layer thicknesses and pass numbers. Fig. 2(b) shows the mode of laser milling of cavity in alumina to investigate the effect of water on machining quality including recast layers and cracks. The scanning interval between machining lines was set as 0.25 mm, which is equal to the radius of laser focused spot. Optical microscopy (Polyvar) was employed to examine the morphology after laser machining and to measure the machining kerf width and depth for the quantitative study. Scanning electron microscopy (SEM, Hitachi S-3400) was used to capture the microstructure of laser machined region. The roughness of machined surface was measured using a Wyko NT1100 white light interferometer. The size distribution of the particles suspending in water during machining was measured by confocal laser scanning microscopy (Olympus OLS-3100) after the suspension was dispersed and dried on a glass substrate.

Table 1
Material properties of 95% alumina used in the work.[31]

Properties	Values
Mass density (kg/m^3)	3720
Specific heat (J/kg K, to 1773 K)	$1044.6 + 1742 \times 10^{-4} \times T - 2796 \times 10^4 \times T^{-2}$
Thermal conductivity (W/m K, to 1573 K)	$5.5 + 34.5e^{[-0.0033\times(T-273)]}$
Elastic module (GPa)	300
Poisson's ratio	0.21
Secant coefficient of thermal expansion (10^{-6} K^{-1})	8.2
Melting point (°C)	2050
Vaporisation point (°C)	2980
Tensile strength (MPa)	220
Compressive strength (MPa)	2600

3. Modelling approaches

In order to understand the effect of water cooling on thermal behaviour in the machining process, a 3D finite element model was developed to simulate the temperature field and resulting stress characteristics during laser machining in air and in water. ANSYS software was employed to solve this transient problem. For the FE transient thermal analysis, it was assumed that the difference between the thermal behaviours for laser machining in air and in water was predominantly governed by the different heat convection coefficients. The heat convection coefficient of water (500–10,000 W/m^2 K) is 2–3 orders higher than that of air (10–100 W/m^2 K).[28] In this work, the heat convection coefficient of water was set as 1000 W/m^2 K, whereas the heat convection coefficient of air was set as 100 W/m^2 K. The heat convection was applied on all the surfaces of the model as a boundary condition. The convection heat loss follows:[32]

$$k\frac{\partial T}{\partial n} = -h(T - T_\infty) \quad (1)$$

where T_∞ and h denote the room temperature and heat convection coefficient, respectively, and n is the normal vector point outward from the surface. The ambient temperatures for air and water were both taken as 27 °C.

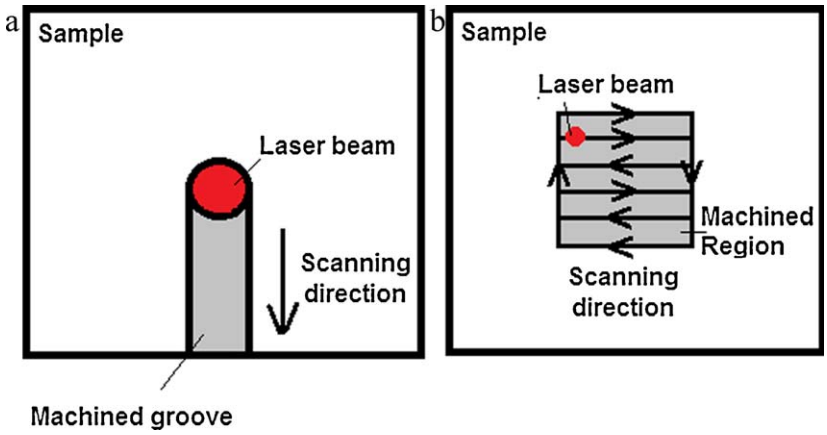

Fig. 2. The machining modes using in this work. (a) Straight line grooves by multi-pass scanning and (b) laser milling of rectangular cavities.

The CO_2 laser beam was assumed to have a TEM_{00} mode and the phase changes during machining were ignored. The FE transient thermal analysis was performed using the same process parameters as in the experiment. The surface heat flux distribution, $I(x, y)$, applied on the surface of workpiece was expressed as

$$I(x, y) = \frac{P_0}{\pi r_0^2} \times e^{-((x^2+y^2)/r_0^2)} \tag{2}$$

where r_0 is the radius of laser spot at focal plane position which was set as 0.5 mm, and P_0 is the laser power arriving at the workpiece surface. Although the 10.6 μm wavelength laser has a static absorption coefficient of about 500 cm^{-1} in water,[33] the Beer-Lambert's law was not used to calculate the value of transmitted laser intensity on workpiece underwater due to complex photo thermal interactions of the laser, water and the workpiece during machining.[28] In the FE model, the P_0 was set as the laser output power. Considering the translational laser beam with a velocity, v, along the x+ direction, Eq. (2) is transformed as.

$$I(x, y, t) = \frac{P_0}{\pi r_0^2} \times e^{-(((x-vt)^2+y^2)/r_0^2)} \tag{3}$$

The governing equation for the simulation of temperature fields has been established by the following heat diffusion equation:[34]

$$\begin{cases} k(T)\left(\dfrac{\partial^2 T(x,y,z,t)}{\partial x^2} + \dfrac{\partial^2 T(x,y,z,t)}{\partial y^2} + \dfrac{\partial^2 T(x,y,z,t)}{\partial z^2}\right) \\ \quad = \rho c(T)\dfrac{\partial T(x,y,z,t)}{\partial t} \\ -k(T)\left(\dfrac{\partial T(x,y,0,t)}{\partial x} + \dfrac{\partial T(x,y,0,t)}{\partial y} + \dfrac{\partial T(x,y,0,t)}{\partial z}\right) \\ \quad = I(x,y,t) \end{cases} \tag{4}$$

where $k(T)$ is the temperature-dependent thermal conductivity, ρ is the material's mass density and $c(T)$ is the temperature-dependent specific heat as listed in Table 1. The initial condition for the model was assumed to be an uniform temperature within the bulk material given as $T(x, y, z, 0) = T_0$, where T_0 is the room temperature, 27 °C.

Based on the temperature field calculated by the FE transient thermal analysis, thermal-stress simulation was performed. In the thermal-stress simulation, the FE model with element SOLID70 for thermal analysis was transformed into the SOLID185 that was used for structural analysis. The boundaries for structural analysis were assumed to be traction-free for all surfaces. However, the elements with the temperature above melting point, i.e. 2050 °C were eliminated before structural analysis in order to simulate the melt pool size and obtain the accurate stress simulation. The thermal-stress was generally considered as the main reason of crack generation and propagation during laser machining of brittle material.[35] For the brittle material, it was assumed that the main mechanism causing crack formation followed the 1st strength theory, i.e. the tensile stress larger than the tensile strength.[36] Therefore, the 1st strength theory was selected in this work as the fracture criterion.

A SPH model was also developed in this work to study the hydrodynamic behaviour of interactions between water and molten material during underwater machining. Using the SPH method, the computational domain was divided into a set of discrete particles. These particles have a spatial distance, known as the smoothing length, over which their properties are smoothed by a kernel function. Different from the standard FE methods, SPH approximates physical quantities of each particle using the kernel function. The most attractive nature of SPH method is that it eliminates the need of computation termination due to the possible large element distortion inherent in Lagrangian formulation based FE methods.[37] Therefore, it is more suitable to simulating the fluid dynamics than the standard FE method.

The fluid in the SPH model was divided, and the properties of each of elements were associated with its centre, which was then interpreted as a particle. A particle i has a mass m_i, position r_i, density ρ_i and velocity v_i. In SPH, the interpolated value of any field, A, at position r is approximated by[38]:

$$A(\vec{r}) = \sum_i m_i \frac{A_i}{\rho_i} W(\vec{r} - \vec{r}_i, h) \tag{5}$$

where W is an interpolating kernel function, h is the interpolation length and the value of A at r_i is denoted by A_i. The sum is over all particles, i with a radius $2h$ of r_i. $W(\vec{r}, h)$ is a spline

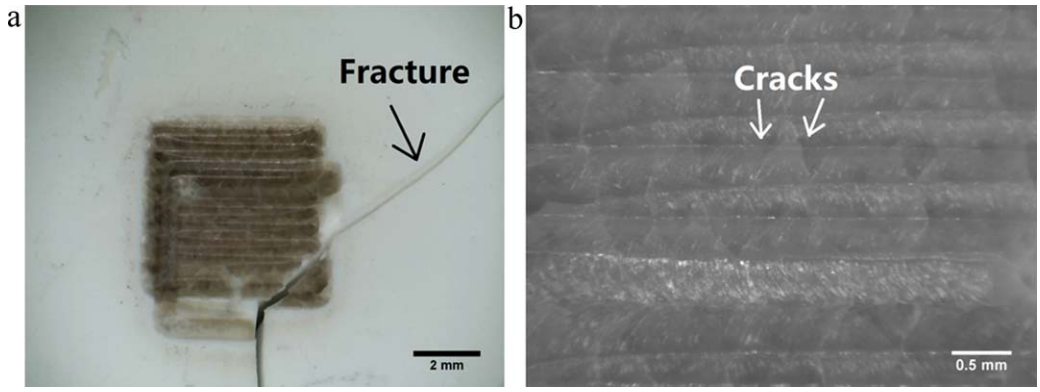

Fig. 3. The optical micrographs of CO_2 laser machined alumina cavity in air at a laser power of 60 W and a speed of 10 mm/s with drawn dimension of 5 mm × 5 mm, in terms of (a) top of the cavity and (b) a close-up view of the recast layer on the bottom surface. The fracture appeared at the 4th scanning cycle.

based interpolation kernel function of radius $2h$, which is a C^2 function that approximates the shape of a Gaussian function and has a compact support. This allows smoothed approximations to the physical properties of the fluid to be calculated from the particle information. Thus, the particle approximation for each particle j can be approximated by summing the contributions of neighbouring particles i as follows:

$$A(\vec{r}_j) = \sum_i m_i \frac{A_i}{\rho_i} W(\vec{r}_j - \vec{r}_i, h) \tag{6}$$

The finial discrete forms of governing equations (i.e. mass, momentum, and energy conservation equations) can be expressed as follows[39]:

$$\begin{cases} \dfrac{d\rho_j}{dt} = \rho_j \sum_i \dfrac{m_i}{\rho_i}(v_i^\alpha - v_j^\alpha)\dfrac{\partial W(x_j - x_i, h)}{\partial x_j^\alpha} \\ \dfrac{dv_j^\alpha}{dt} = -\sum_i m_i \left(\dfrac{\sigma_j^{\alpha\beta}}{\rho_j^2} + \dfrac{\sigma_i^{\alpha\beta}}{\rho_i^2}\right)\dfrac{\partial W(x_j - x_i, h)}{\partial x_j^\beta} \\ \dfrac{dE_j}{dt} = -\dfrac{\sigma_j^{\alpha\beta}}{\rho_j^2}\sum_i m_i(v_j^\alpha - v_i^\alpha)\dfrac{\partial W(x_j - x_i, h)}{\partial x_j^\beta} \end{cases} \tag{7}$$

where t donates the time, x is the spatial coordinate, v^α is the velocity component, $\sigma^{\alpha\beta}$ is the stress tensor component, E is the specific internal energy, and the subscripts α ($\alpha = 1, 2, 3$) and β ($\beta = 1, 2, 3$) are the component indices. Simulation solutions were obtained by solving Eq. (7) in conjunction with equations of state, material models and initial and boundary conditions. This problem was solved by commercially available explicit CFD software AUTODYN (issued by ANSYS Inc.).

4. Results and discussion

4.1. Effect of water cooling

Based on initial experimental trails, it was found at a laser power of 60 W and scanning speed of 10 mm/s, high quality machining of alumina ceramic can be realised, in which the heat damage and recast layer were reduced to a low level and the machining rate was relatively high compared with other parameters. Fig. 3(a) shows the top-view of CO_2 laser machined alumina cavity in air at a power of 60 W, a speed of 10 mm/s and 4 scanning cycles with a dimension of 5 mm × 5 mm. It was found that fracture appeared frequently during machining in air below 10 scanning cycles due to the high thermal-stress caused by the large amount of accumulated heating energy.[40] The discoloured recast layer on the bottom surface indicated the high temperature (>3500 °C) during laser machining in air resulting in many sub-oxides of aluminium generated.[34] The micrograph of the recast layer on the bottom surface is shown in Fig. 3(b). It can be found that micro-cracks appeared in the recast layer and formed a fine crack network, which indicates that the thermal damages in processing region were serious during laser machining in air.

Fig. 4 shows the cross-section SEM micrographs of the machined cavity in air. It can be found that the recast layer on the bottom of the cavity was significant and a crack propagated into the base material (Fig. 4(a)), which could lead to a fracture of the workpiece as the side surface indication. Fig. 4(b) shows the microstructure of recast layer. The alumina grains in the recast layer re-grew to be columnar along the direction of the incident laser, in which the crack propagated along the grain boundary. Fig. 4(c) shows a smooth recast layer surface on the bottom of the cavity, where the micro-cracks appeared due to the serious heat damages as the micrograph captured by optical microscopy (Fig. 3(b)).

The CO_2 laser underwater machined alumina cavity using the same process parameters is shown in Fig. 5. The thickness of the water layer is about 4 mm above the top surface of workpiece and 50 scanning cycles were applied for the 1-mm deep cavity. Fracture and cracks were suppressed in the underwater machining as shown in Fig. 5, which demonstrates that the water cooling was beneficial to preventing heat damages.

Fig. 6 shows the cross-section SEM micrographs of the machined cavity. It can be found that the recast layer was insignificant and the side wall surface was smooth in underwater machining as shown in Fig. 6(a). Fig. 6(b) shows the microstructure of recast layer, in which the alumina grains had no significant change but a porous structure was formed. The porous structure could reduce the strength of recast layer and base material, by which the recast layer could be easily removed via mechanical

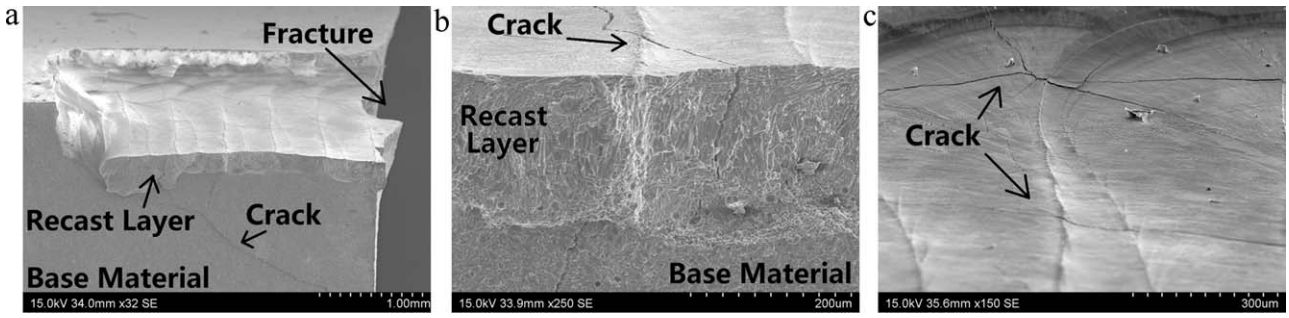

Fig. 4. The SEM micrographs of CO_2 laser machined alumina cavity in air. (a) An overview of the cavity cross-section, (b) a close-up view of the recast layer cross-section on the bottom of the cavity and (c) a close-up view of the recast layer surface on the bottom of the cavity.

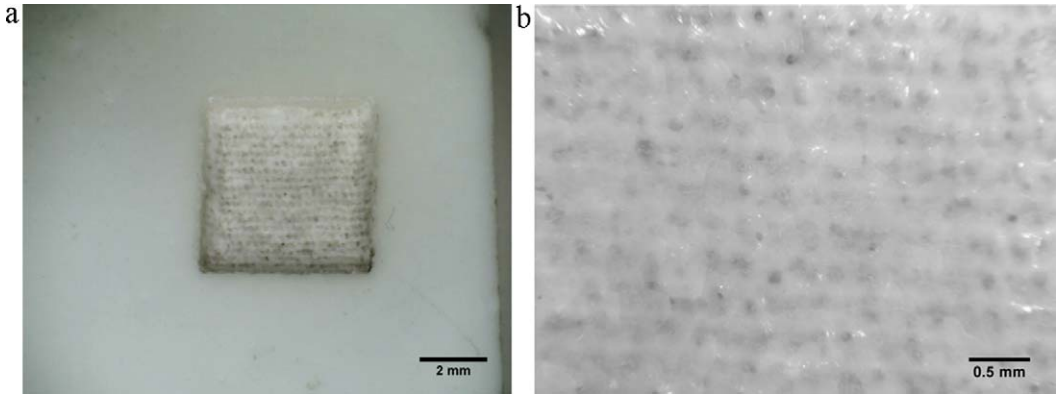

Fig. 5. The optical micrographs of CO_2 laser machined alumina cavity in water at a power of 60 W, a speed of 10 mm/s and 50 scanning cycles with drawn dimension of 5 mm × 5 mm. (a) Top of the cavity and (b) a close-up view of the recast layer on the bottom surface. The thickness of water layer is about 4 mm.

post-processing. Fig. 6(c) shows the recast layer surface on the bottom of the cavity, where micro-cracks were suppressed but the roughness was increased due to the obvious voids. The difference in the microstructures of recast layer formed by machining in air and in water indicates that the water has a significant effect on chilling of the machined region.

In order to understand the difference in thermal behaviours during laser machining in air and in water, an FE thermal and structural analysis was performed. Fig. 7 shows the difference of temperature and thermal-stress distributions between machining in air and in water. It reveals that, with the same process parameters, underwater machining produced a lower maximum temperature and smaller HAZ than machining in air (Fig. 7(a) and (b)) and hence the maximum thermal-stress was reduced in underwater machining (Fig. 7(c) and (d)), which was in agreement with previous studies using analytical solutions.[28,29] In order to further investigate the thermal behaviour in different ambient conditions, the FE simulated temperature and thermal-stress distribution along the machining path across the melt pool was plotted as shown in Fig. 8. It can be found that the melt pool in water was smaller than that in air. The low maximum temperature and steep temperature gradient in water produced a smaller HAZ compared with that in air. Fig. 8(b) highlights the lower compressive and tensile stress peaks in underwater machining. During machining in air, the two tensile stress peaks near the melt pool are greater than those in water, which implies that

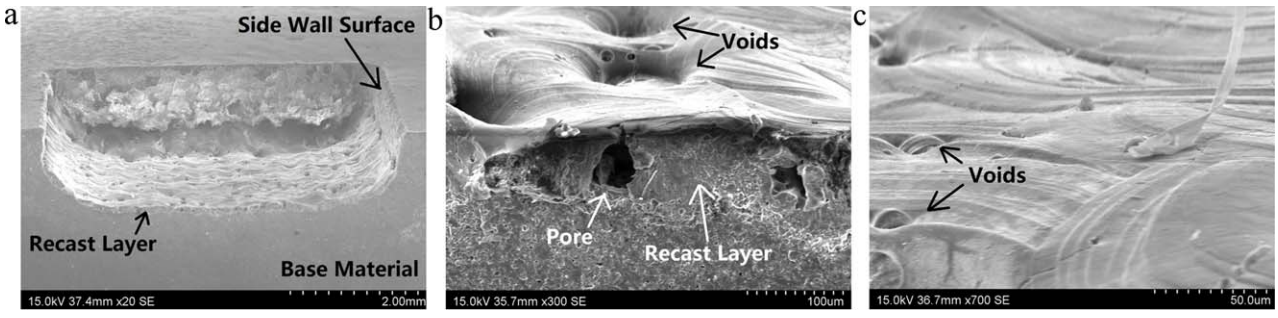

Fig. 6. The SEM micrographs of CO_2 laser machined alumina cavity in water. (a) An overview of the cavity cross-section, (b) a close-up view of the recast layer cross-section on the bottom of the cavity and (c) a close-up view of the recast layer surface on the bottom of the cavity.

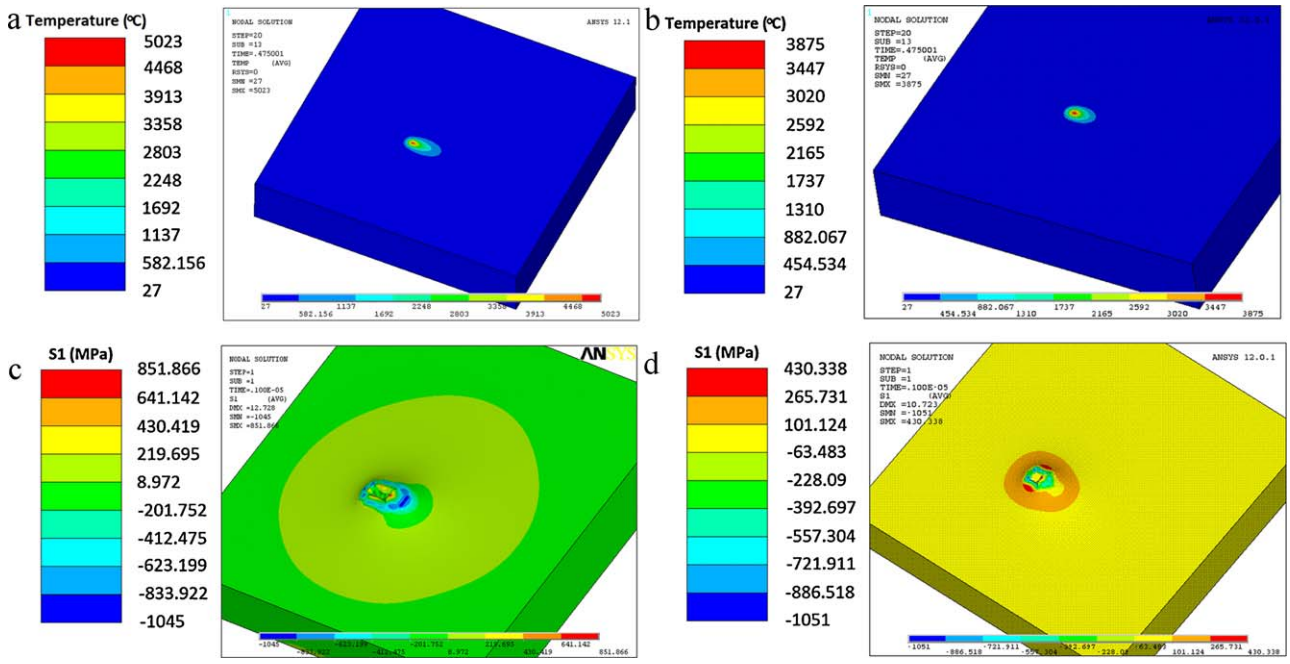

Fig. 7. Temperature fields and resulting stress distributions during laser machining in different ambient conditions. (a) Temperature field during laser machining in air, (b) temperature field during laser underwater machining, (c) thermal–stress distribution during laser machining in air, and (d) thermal–stress distribution in laser underwater machining.

cracking in air machining could be more easily initiated than that in underwater machining due to higher heat energy diffused into the base material. The tensile stress in front of melt pool could induce the crack formation and propagation into the base material to cause the fracture as shown in Fig. 3(a), whereas the tensile stress behind the melt pool induces cracking during molten material resolidification (as shown in Fig. 3(b)). Obviously, the two tensile stress peaks were suppressed in underwater machining (as shown in Fig. 8(b)).

4.2. Effect of fluid dynamics

Fig. 9 shows the schematic diagram of interaction between the CO_2 laser beam, water, and the alumina substrate during underwater machining. When the laser was delivered onto the water surface, a portion of the laser energy was absorbed by water, in which a rapid heating and vaporisation process was induced due to the high absorption of the water with respect to the 10.6 μm wavelength CO_2 laser.[30] During this process, many

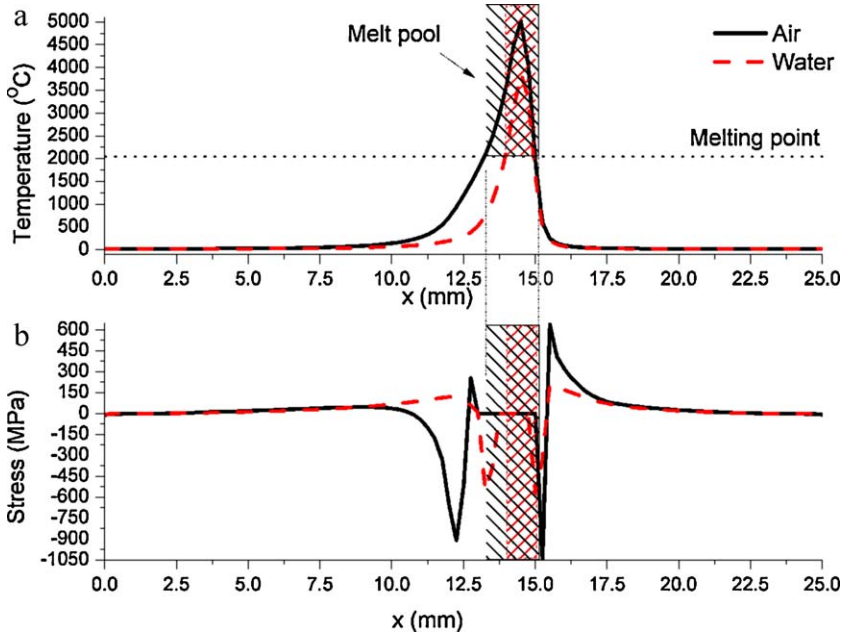

Fig. 8. (a) Temperature fields and (b) 1st principle stress distributions along machining path during laser machining of alumina in air and in water ambient.

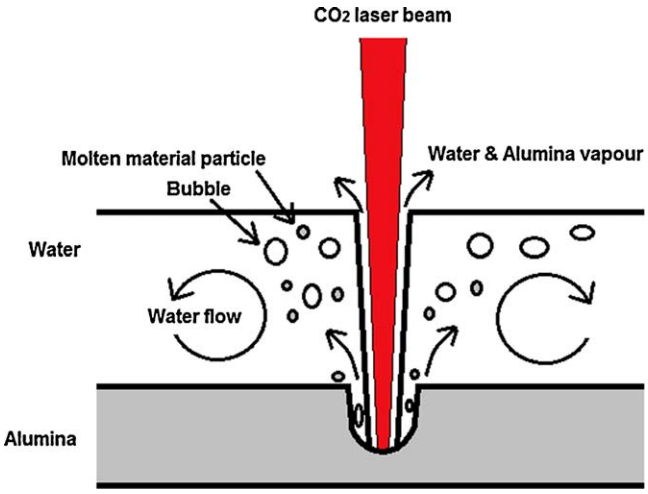

Fig. 9. Schematic diagram of interaction between the CO_2 laser beam, water, and alumina substrate.

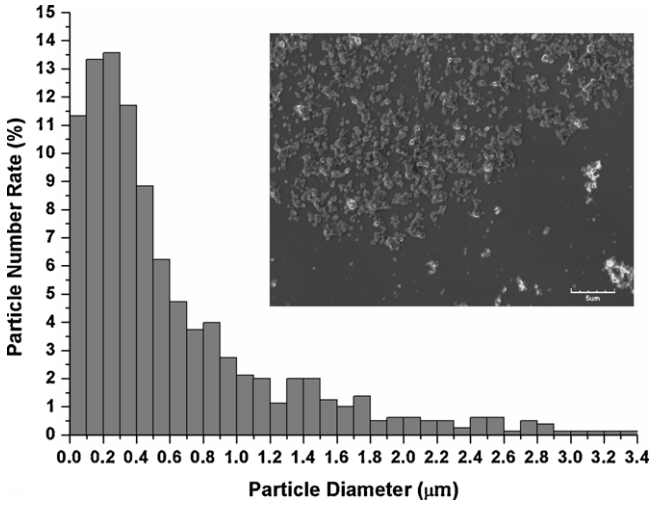

Fig. 11. Histogram of the size distribution of the particles generated in laser underwater machining.

bubbles are generated and a keyhole in water was formed as a channel for the other portion of energy penetrating.[41] The energy arrived onto the surface of alumina was absorbed to melt and/or vaporise the workpiece surface. The molten material was ejected from the machining region into the water due to the inherent recoil pressure induced in the keyhole of the workpiece, as well as the water vapour pressure. Then, the ejected molten particles were removed by the water flow (as shown in Fig. 9).

Fig. 10 shows the photographic images of the interaction between laser beam and water in the experiments. Fig. 10(a) shows the water wave caused by the water evaporation, which is important for molten particles removal from the machining region. Fig. 10(b) shows the bubble formation during laser vaporising of water. The mean diameter of these bubbles is about 0.9 mm.

During underwater machining, the velocity of the ejected particles is much lower than that in air due to the presence of viscose fluid, which would prevent the debris deposition. Therefore the debris suspends in the water with a relatively long time. The size distribution of the particles generated in laser underwater machining is shown as Fig. 11, in which the measured particle number is up to 1000 shown in the inserted micrograph. The mean diameter of these particles is 220 nm. The histogram shows that the number of the particles with the diameter up to 500 nm is more than 50% of the total measured particle number. It indicates that the major size distribution of the particles generated in CO_2 laser underwater machining was in sub-microns.

The high recoil pressure caused by water evaporation would benefit to prevent the recast and dross formation. Fig. 12 shows the side wall surface of machined groove in air and in water, respectively. Dross was evident on the side wall surface and a significant recast layer was on the bottom of machined groove for machining in air. However, these defects were eliminated by underwater machining (as Fig. 12(b)), in which the side wall surface was smooth and the recast layer on the bottom of groove was insignificant.

Fig. 13 further shows the microstructure of the side wall surface and the bottom of the machined groove in air and in water, respectively. The grains in dross were mainly glassy phases as shown in Fig. 13(a), which indicated that the molten material was resolidified on the side wall surface during laser machining in air. During machining in water, the grains on side wall surface were almost same as the base material and a few of grains

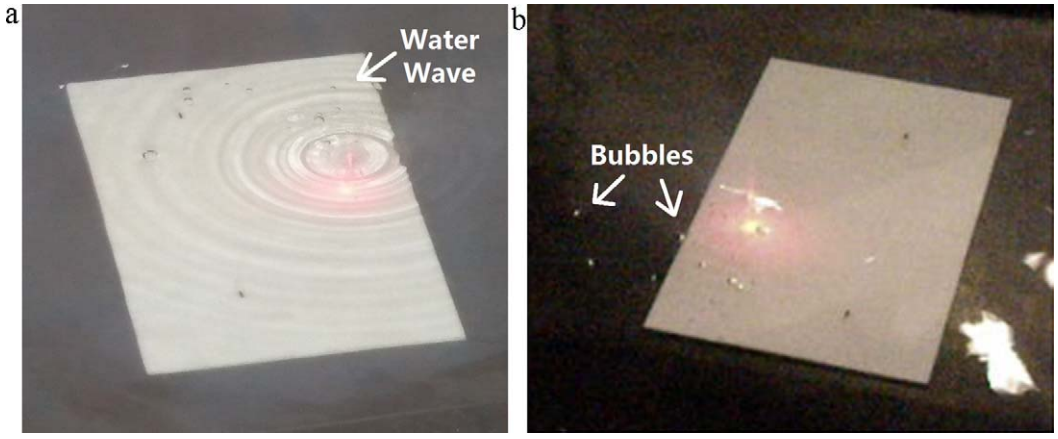

Fig. 10. Capture of (a) water wave and (b) bubble formation during the interaction between CO_2 laser beam and water in experiments.

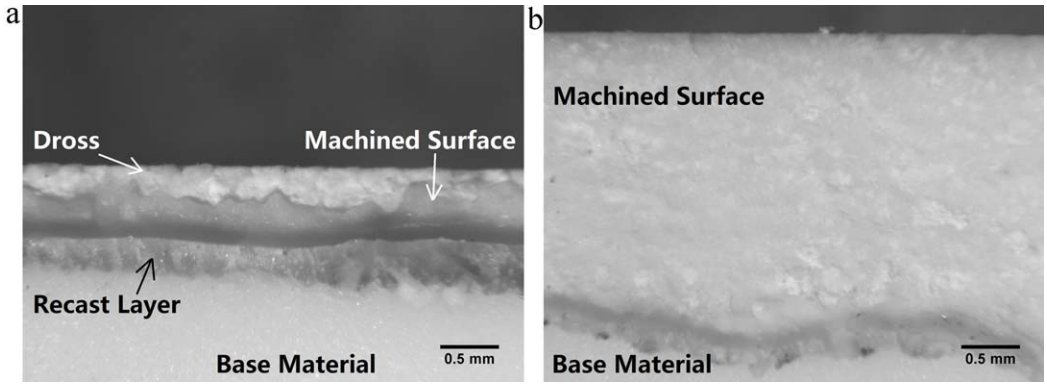

Fig. 12. Side wall surface of the groove machined (a) in air and (b) in water.

were melted (as shown in Fig. 13(b)). This is due to the high recoil pressure produced in water to prevent the molten material resolidification. Fig. 13(c) and (d) show the microstructure of recast layer on the bottom of the groove machined in air and in water, respectively. The results were same as those of machined cavity as shown in Figs. 4(b) and 6(b), i.e. the significant recast layer with columnar grains formed during machining in air and the porous structure produced in recast layer during underwater machining.

Fig. 14 shows the roughness of the side wall surfaces machined in air and in water. The arithmetical mean roughness (R_a) of the side wall surface machined in air ($R_a = 13.16\ \mu m$) is approximately 1.5 times higher than that of the side wall surface machined in water ($R_a = 5.12\ \mu m$). The average maximum height of the profile (R_z) of the side wall surface machined in air ($R_z = 43.68\ \mu m$) is about twice that of the side wall surface machined in water ($R_z = 23.02\ \mu m$). This is due to the dross adhered onto the side wall surface during machining in air. The dross increased the surface roughness as the bulge appeared in roughness plot (Fig. 14(a)). The measured surface roughness validated that the underwater machining can prevent dross adhesion and process a smoother side wall surface than that machined in air.

Fig. 15 shows the cross-section of machined groove in air and in water. The crack and fracture appeared after few passes during machining in air (as Fig. 15(a)). However, the groove machined in water had relatively high quality (as Fig. 15(b)), demonstrating a high aspect ratio and crack-free machining.

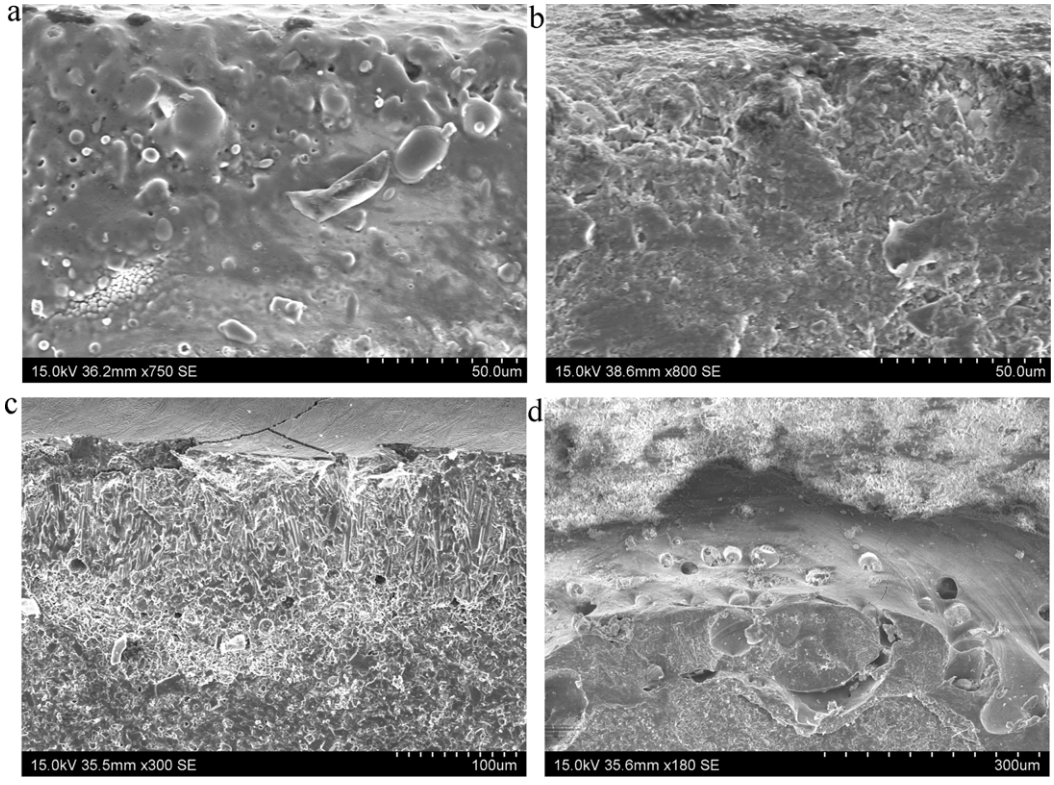

Fig. 13. Microstructure of dross on the side wall surface of the groove machined (a) in air and (b) in water and cross-section microstructure of recast layer on the bottom of the groove machined (c) in air and (d) in water.

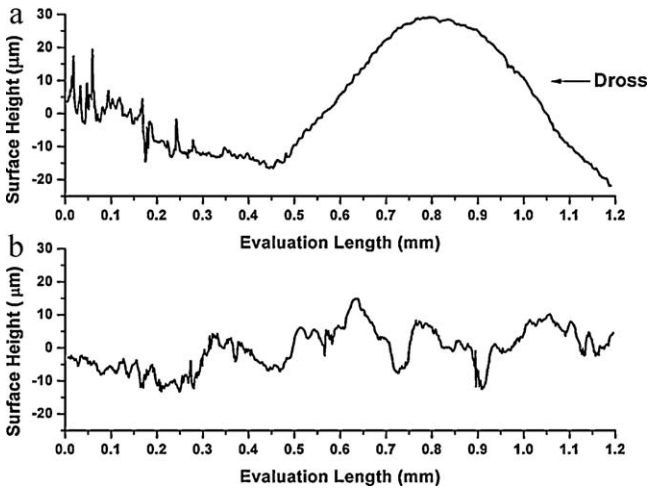

Fig. 14. Roughness plot of the side wall surface of the groove machined (a) in air (R_a = 13.16 μm, R_z = 43.68 μm) and (b) in water (R_a = 5.12 μm, R_z = 23.02 μm).

In order to understand the empirical hypothesis of the effect of fluid dynamics (as shown in Fig. 9), a 2D fluidic transient smooth particle hydrodynamic (SPH) model was developed. Fig. 16(a) is the setup of the SPH model. The model was simplified to only consider the process of melt ejection rather than the energy absorption and phase transition due to the complicate process of laser process and the limitation of the software. It was assumed that the melt pool was formed for the developed model and the molten material was ejected by the recoil pressure existed in the melt pool. The initial velocity of the melt ejection was set as 20 m/s.[42]

Fig. 16 shows the process of melt ejection from the keyhole during underwater machining. It was found that part of the molten material was injected into the water and the other part was ejected out together with some water (as shown in Fig. 16(c) and (d)). The bubbles were also formed in water as depicted in Fig. 16(d). The simulated results implied that the melt ejection perturbed the water and may cause turbulence and laminar flows in water.

Fig. 17 shows the fluidic velocity caused by melt ejection in underwater machining. It can be found that the maximum velocity was concentrated on the region near the ejecting front and the water was pushed away from the ejecting path as shown in Fig. 17(a). Fig. 17(b) and (d) illustrates the details of water flow characteristic under various water depths. The flow vector close to water surface was directed to the normal of the water surface (as Fig. 17(b)), which indicated that the water in this region would flow to the water surface and hence cause ripples on water surface. The laminar flow appeared at the middle of the water depth (as Fig. 17(c)), by which the injected molten particles would be carried away resisting to re-depositing on the machined region. Fig. 17(d) shows the flow characteristic near the machined region, which demonstrates the initial turbulence formation of water flow. It was useful to induce the water into the machined groove for chilling. The SPH simulated result shows the significance of water flow for underwater machining, which was in agreement with the empirical hypothesis as shown in Fig. 9.

4.3. Effect of scanning pass number and water layer thickness

The process efficiency of underwater machining depends on the number of laser scanning cycles and the thickness of water layer above the workpiece surface. Fig. 18 shows the effect of water layer thickness on the machined kerf width and depth in alumina substrate at a fixed 60 W laser power and 10 mm/s scanning speed for 1–100 passes. It can be seen that the kerf depth increases with the pass number but decreases with increasing water layer thickness as shown in Fig. 18(a). The kerf width reduces with the water layer thickening but keeps similar widths for different passes at the same water layer thickness as shown in Fig. 18(b). It indicates that the water layer thickness is a significant parameter to determine the machining kerf width due to the laser energy arriving on the workpiece surface varying with the water layer thickness, whereas the number of passes governs the machined depth together with water layer thickness. Fig. 19 shows the average machining rate, i.e. depth divided by the pass number, which reveals that the depth rate exponentially decreases with increasing number of passes. When the pass number was up to 100, the machining rate approached a constant that was only determined by the water layer thickness, where the depth rate decreased with increasing water layer thickness.

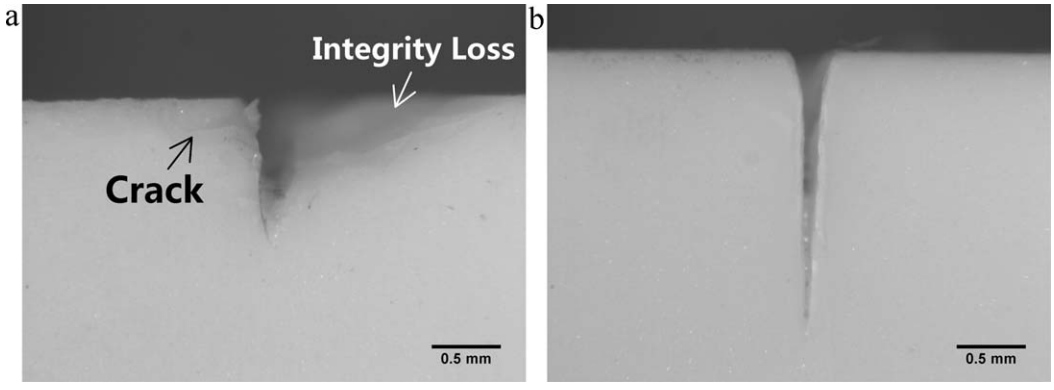

Fig. 15. Cross-section of the groove machined (a) in air at a power of 60 W and a scanning speed of 10 mm/s for 4 passes and (b) in water at a power of 60 W and a scanning speed of 10 mm/s for 80 passes.

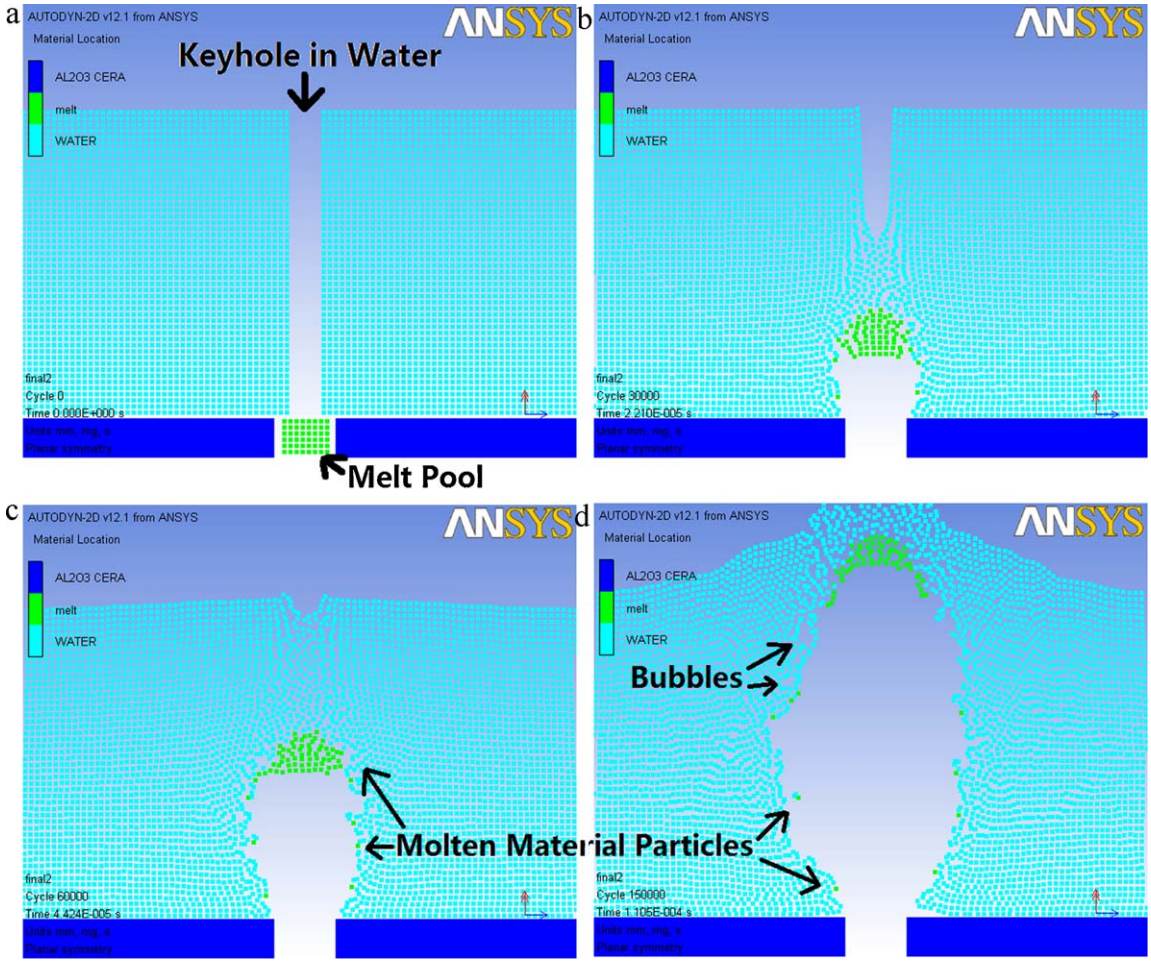

Fig. 16. Time history of melt ejection during underwater machining at (a) 0 μs, (b) 22.1 μs, (c) 51.6 μs and (d) 110 μs.

For deep cavity machining, multi-pass is essential and hence the process efficiency is mainly determined by the thickness of water layer. For a thin water layer (<2 mm), the water cannot always wet the alumina surface during machining, which could cause a poor cooling effect and induce crack initiation around the machining region. However, when the water layer was greater than 5 mm, the machining rate was below 15 μm/pass at 60 passes or more, which was undesirable due to the low process efficiency. The thickness of water layer is suggested at 3–4 mm in the work, which could balance a good surface cooling effect and a high machining efficiency. Also the thickness of water layer provided an adequate space to remove molten material particles. As shown in Fig. 19 the average machining rate for this water layer thickness is always greater than 20 μm/pass at 60 W laser power and 10 mm/s scanning speed.

4.4. Laser underwater machining of polygon cavities

Based on the parameters discussed above, some polygon cavities were machined underwater at a water layer thickness of 4-mm, a laser power of 60 W and a scanning speed of 10 mm/s for 100 scanning cycles. Fig. 20 shows the optical micrographs of CO_2 laser underwater machined alumina polygon cavities. The crack-free machining of polygon cavities in alumina with smooth machined side wall surfaces was achieved by the CO_2 laser underwater machining. The thickness of these polygon cavities is up to 2.36 mm.

The typical machining time for a square cavity with dimension of 5 mm × 5 mm × 2.36 mm was about 30 min. Therefore, the average machining rate for underwater machining with 60 W laser power and 10 mm/s feed rate at 4 mm thick water layer was 2.95 mm^3/min. Based on the experimental data in Fig. 19, the machining rate at the first machining circle (i.e. the first scanning cycle for whole cavity pattern scanning) should be 18.75 mm^3/min, which is close to pulsed laser machining in air.[4] However, the machining rate reduces when the machined depth of cavity increases as the water layer becomes thicker as illustrated in Fig. 21. Therefore, the equivalent machining rate was reduced.

4.5. Potential improvements for high process efficiency and quality

In order to further improve the process efficiency, substrate position correction technique should be developed for con-

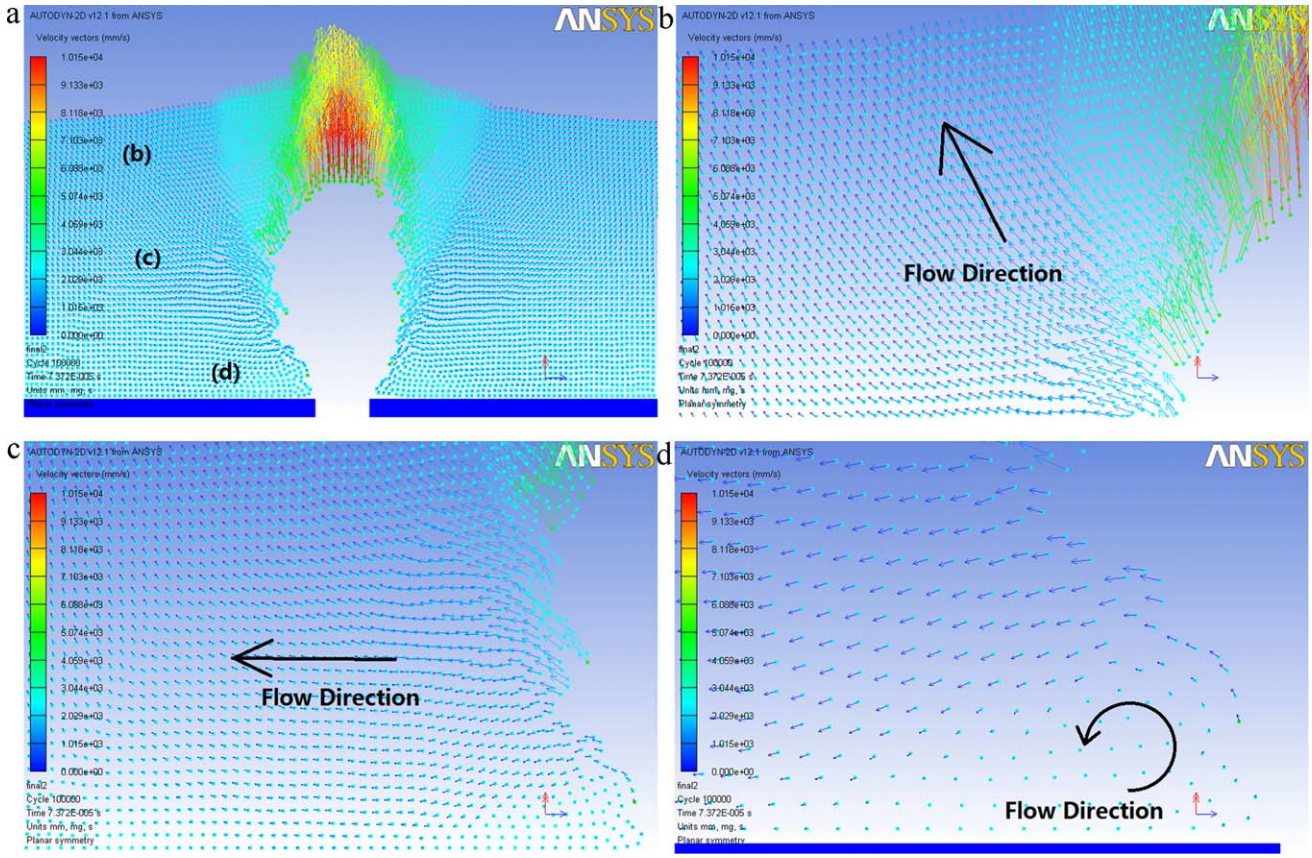

Fig. 17. The overview vector plot (a) of water flow during underwater machining and the detailed view at the region (b) near water surface, (c) at the middle of water depth, and (d) near the machined region.

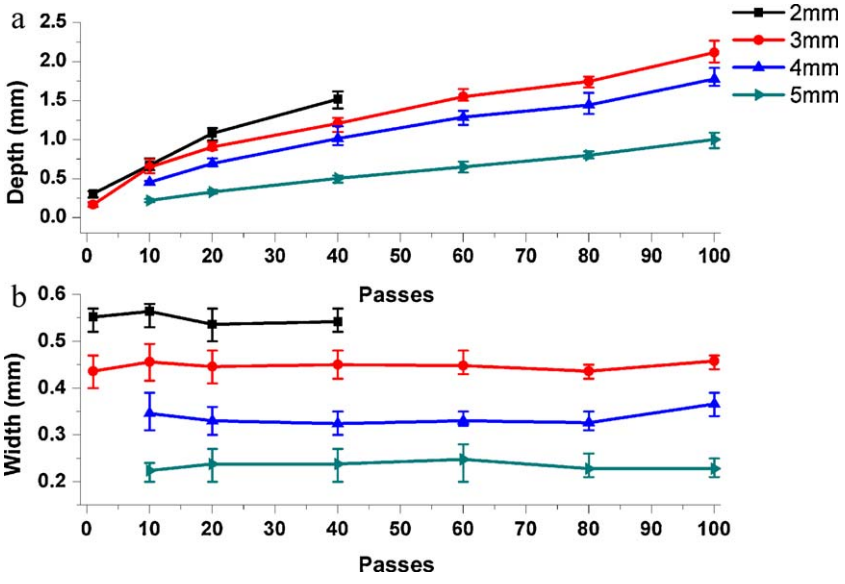

Fig. 18. The effect of water layer thickness on machining (a) depth and (b) width in alumina substrate at a fixed 60 W laser power and 10 mm/s scanning speed for 1–100 passes.

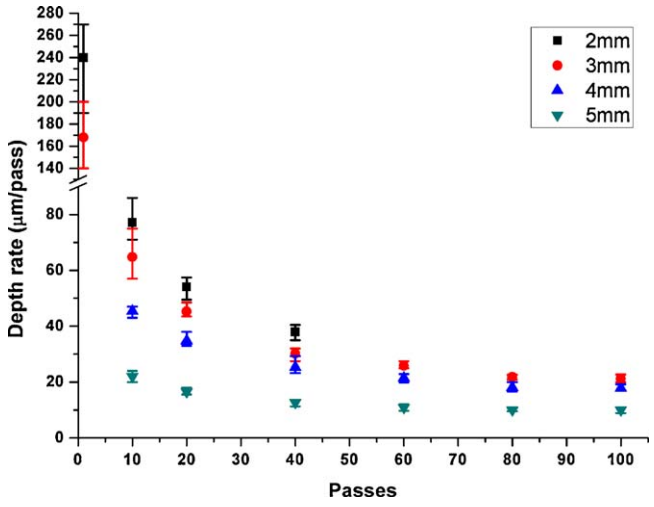

Fig. 19. The effect of water layer thickness on machining rate in alumina substrate at a fixed 60 W laser power and 10 mm/s scanning speed for 1–100 passes.

sistent water layer thickness with respect to machining site throughout the machining process. The position of the workpiece is corrected as the successive passes proceed. However, the maximum machining depth using this method is limited by the thickness of water layer above the workpiece surface, i.e. 4 mm under the current optimised experimental setup. When the machining depth is greater than this value, part of unmachined workpiece surface will be higher than the water surface, under which condition the water cannot spontaneously flow into the closed cavities for chilling and heat damages will occur.

Therefore, the forced water layer formation technique should be developed for deeper closed cavities machining. The schematic diagram of the process setup is shown in Fig. 22. A water jet is applied to form a water layer on the workpiece top-surface. The layer thickness is primarily determined by the water flow rate employed. This setup can also solve the problem of the suspending particles scatter and absorb the laser light during still-water machining, as the water continuously flows under the high water pressure and a liquid circulation with filtration is employed. The substrate position correction is applied at the same time in order to meet the focal plane position. The feasibility of this technique will be verified in our future work.

In addition to the pure water used in this work, other liquids (e.g. salt, basic or acid solutions) have been used in previous studies for chemical-assisted laser machining of hard-to-machined materials. Compared with conventional laser thermal machining, little thermal damage is induced in chemical-assisted laser machining. Alumina ceramic is a compound made up of aluminium atoms and oxygen atoms, which are in a very tight array (i.e. hexagonal atomic structure in grains). Therefore, alumina ceramic has a good corrosion resistance against most of salts, bases and acids. However, the grain boundaries could be easily etched since the glass phases and inclusions exist.[43] Furthermore, the laser activated photo-chemical and thermal-chemical reactions may also occur within the machining site to enhance the etching efficiency. In previous studies, chemical-assisted laser micromachining, involving laser processing within salt solution,[43] basic solution[44] and acid solution,[45,46] has been found to be able to produce smoother finished surfaces without any detectable HAZ or recast layer than conventional laser thermal machining. The same results were also found in laser wet etching of alumina and its composite.[44,45] In order to introduce

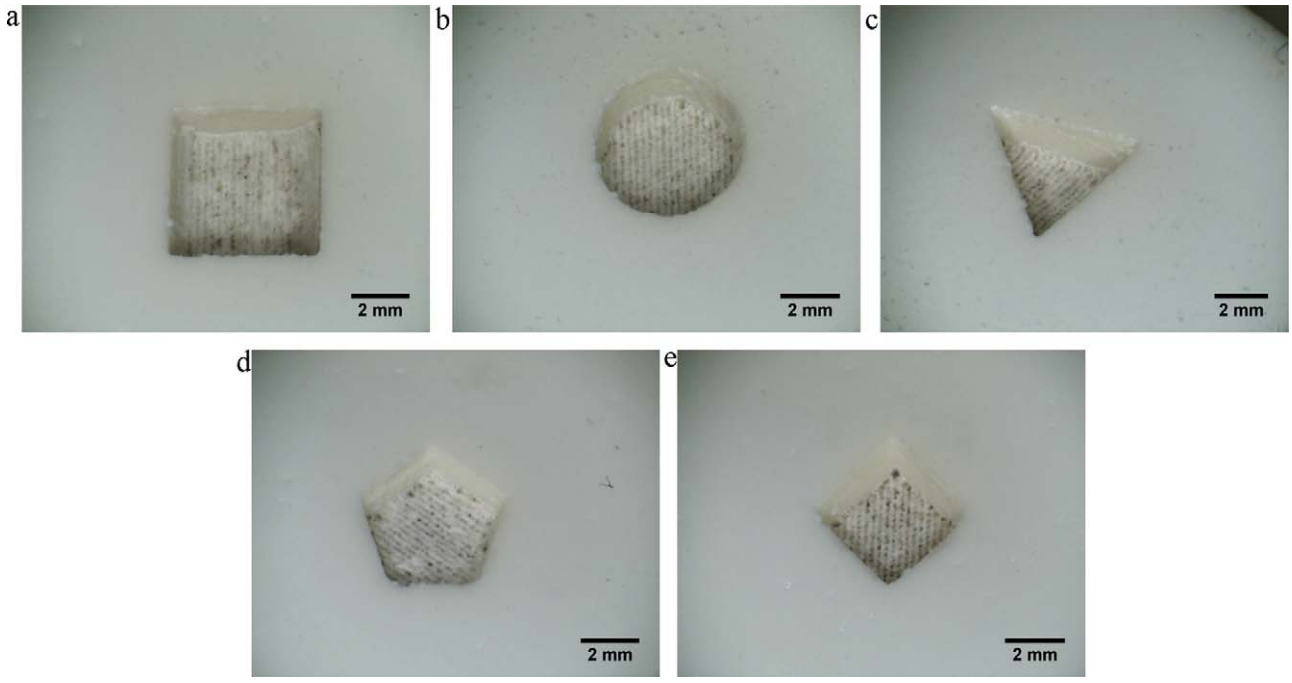

Fig. 20. Optical micrographs of laser underwater machined polygon cavities including (a) square cavity, (b) circular cavity, (c) triangular cavity, (d) pentagon cavity, and (e) prismatic cavity.

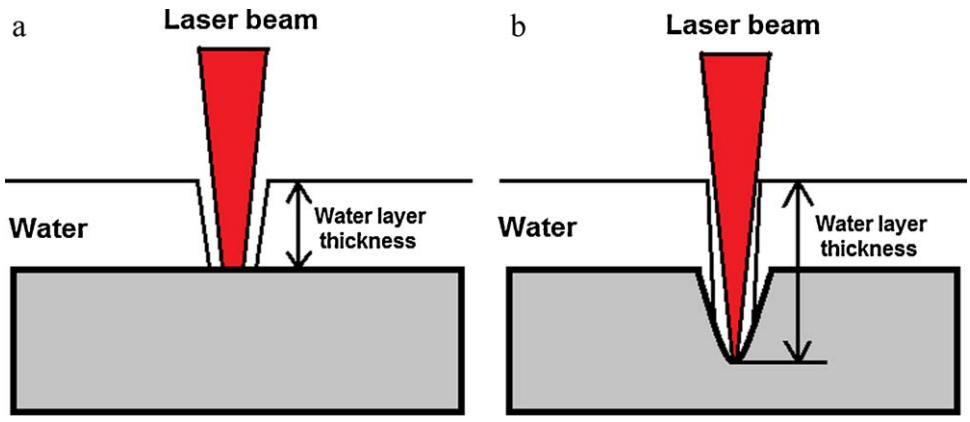

Fig. 21. Schematic diagram of the change of water layer thickness with the depth of cavity increasing. (a) The first pass and (b) the *n*-th pass.

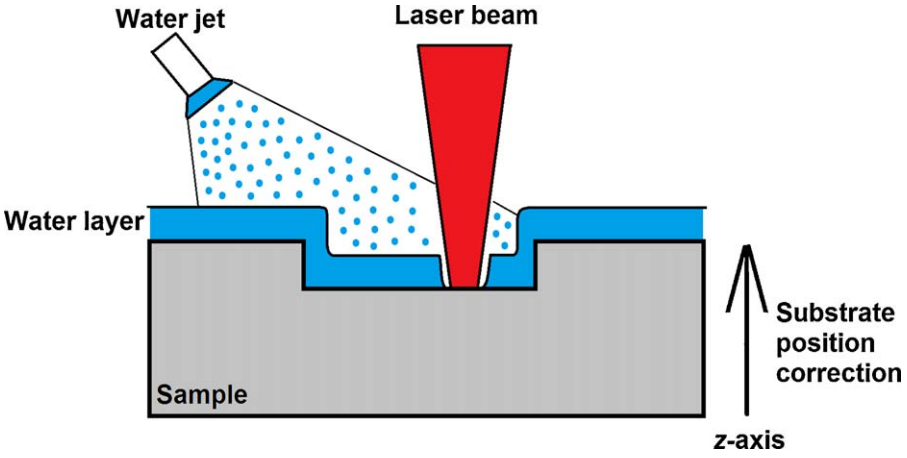

Fig. 22. Schematic diagram of forced water layer formation technique with substrate position correction.

these advantages of laser wet etching into high average power laser machining, chemical-assisted laser macro-machining of structural ceramics will be investigated in our future work.

5. Conclusions

The CO_2 laser underwater machining was successfully demonstrated for crack-free milling the mm-deep cavities in alumina. It was found that the process quality in underwater machining is much better than that in air. Underwater machining has the capability of preventing the crack initiation and reducing heat damages due to the water cooling effect. ANSYS software was employed to understand the mechanism of crack resistance in underwater machining. The differences in the temperature and resulting stress distributions during laser machining in air and in water were studied by the FE model, in which the crack formation was predicted via the 1st principal strength theory. The simulated results were in agreement with the experiments. SPH modelling of interactions between water and molten material ejection shows the behaviour and significance of water flow in the underwater machining process. The machined side wall surface in water was much smoother than in air as the effect of water dynamics produced a high recoil pressure in machining region to eject the molten material from the cavity and prevent recast formation. The effect of water layer thickness and scanning cycle number was studied in this work. It was found that the kerf width was governed by water layer thickness whereas the kerf depth was controlled by the scanning cycle number together with the water layer thickness. The optimal water layer thickness was proposed to be 3–4 mm above the surface of workpiece to guarantee a sufficient cooling effect and a high material removal rate. Also the thickness of water layer provided an adequate space to remove molten material particles. Based on the optimised parameters, several polygon cavities were demonstrated by underwater machining at 100 scanning cycles, 60 W laser power and 10 mm/s scanning speed with a scanning line interval of 0.25 mm. The average machining depth is greater than 2-mm and the machining rate is up to 2.95 mm^3/min.

Acknowledgements

The authors acknowledge the support offered by Institute of Laser Engineering, Beijing University of technology and the joint support of National Science Foundation of China (50875006), Scientific Research Common Program of Beijing Municipal Commission of Education (KM200810005006), Beijing Natural Science Foundation (2082005), and Beijing Nova Program (2006B11).

References

1. Barnes C, Shrotriya P, Molian P. Water-assisted laser thermal shock machining of alumina. *Int J Mach Tool Manuf* 2007;**47**:1864–74.
2. Ji L, Yan Y, Bao Y, Jiang Y. Crack-free cutting of thick and dense ceramics with CO_2 laser by single-pass process. *Opt Laser Eng* 2008;**46**(10): 785–90.
3. Nisar S, Li L, Sheikh MA, Pinkerton AJ. The effect of continuous and pulsed beam modes on cut path deviation in diode laser cutting of glass. *Int J Adv Manuf Technol* 2010;**49**:167–76.
4. Wang C, Zeng X. Study of laser carving three-dimensional structures on ceramics: quality controlling and mechanisms. *Opt Laser Technol* 2007;**39**(7):1400–5.
5. Wang X, Shephard JD, Dear FC, Hand DP. Optimized nanosecond pulsed laser micromachining of Y-TZP ceramics. *J Am Ceram Soc* 2008;**91**(2):391–7.
6. Dear FC, Shephard JD, Wang X, Jones JDC, Hand DP. Pulsed laser micromachining of yttria-stabilized zirconia dental ceramic for manufacturing. *Int J Appl Ceram Technol* 2008;**5**(2):188–97.
7. Parry JP, Shephard JD, Dear FC, Jones N, Weston N, Hand DP. Nanosecond-laser postprocessing of millisecond-laser-machined zirconia (Y-TZP) surface. *Int J Appl Ceram Technol* 2008;**5**(3):249–57.
8. Tsai CH, Chen HW. Laser milling of cavity in ceramic substrate by fracture-machining element technique. *J Mater Process Technol* 2003;**136**:158–65.
9. Tsai CH, Chen HW. The laser shaping of ceramic by a fracture machining technique. *Int J Adv Manuf Technol* 2004;**23**:342–9.
10. Parry JP, Shephard JD, Hand DP. Laser micromachining of zirconia (Y-TZP) ceramics in the picosecond regime and the impact on material strength. *Int J Appl Ceram Technol* 2011;**8**(1):163–71.
11. Perrie W, Rushton A, Gill M, Fox P, O'Neill W. Femtosecond laser microstructuring of alumina ceramic. *Appl Surf Sci* 2005;**248**:213–7.
12. Tian Y, Shin YC. Thermal modeling for laser-assisted machining of silicon nitride ceramics with complex features. *J Manuf Sci E-Trans ASME* 2006;**128**(2):425–34.
13. Chang CW, Kuo CP. An investigation of laser-assisted machining of Al_2O_3 ceramics planing. *Int J Mach Tool Manuf* 2007;**47**:452–61.
14. Lei S, Shin YC, Incropera FP. Experimental investigation of thermo-mechanical characteristics in laser-assisted machining of silicon nitride ceramics. *J Manuf Sci E-Trans ASME* 2001;**123**:639–46.
15. Rebro P, Shin YC, Incropera FP. Design of operating conditions for crackfree laser-assisted machining of mullite. *Int J Mach Tool Manuf* 2004;**44**:677–94.
16. Pfefferkorn FE, Shin YC, Tian Y, Incropera FP. Laser-assisted machining of magnesia-partially stabilized zirconia. *J Manuf Sci E-Trans ASME* 2004;**126**(1):42–51.
17. Sun S, Brandt M, Dargusch MS. Thermally enhanced machining of hard-to-machine materials – a review. *Int J Mach Tool Manuf* 2010;**50**(8): 663–80.
18. Tian Y, Wu B, Anderson M, Shin YC. Laser-assisted milling of silicon nitride ceramics and Inconel 718. *J Manuf Sci E-Trans ASME* 2008;**130**(3), 031013-1-031013-9.
19. Shen X, Lei S. Experimental study on operating temperature in laser-assisted milling of silicon nitride ceramics. *Int J Adv Manuf Technol* 2010 [published online].
20. Shen X, Lei S. Thermal modeling and experimental investigation for laser assisted milling of silicon nitride ceramics. *J Manuf Sci E-Trans ASME* 2009;**131**(5), 051007-1-051007-10.
21. Yang B, Lei S. Laser-assisted milling of silicon nitride ceramic: a machinability study. *Int J Mech Manuf Syst* 2008;**1**(1):116–30.
22. Morita N, Ishida S, Fujimori Y, Ishikawa K. Pulsed laser processing of ceramics in water. *Appl Phys Lett* 1988;**52**(23):1965–6.
23. Kruusing A. Underwater and water-assisted laser processing. Part 1. General features, steam cleaning and shock processing. *Opt Laser Eng* 2004;**41**(2):307–27.
24. Kruusing A. Underwater and water-assisted laser processing. Part 2. Etching, cutting and rarely used methods. *Opt Laser Eng* 2004;**41**(2):329–52.
25. Muhammad N, Whitehead D, Boor A, Li L. Comparison of dry and wet fibre laser profile cutting of thin 316L stainless steel tubes for medical device applications. *J Mater Process Technol* 2010;**210**(15):2261–7.
26. Qi L, Wang Y, Yang L. Study of Nd:YAG pulsed laser milling Al_2O_3 ceramic in water and air condition. *Int Technol Innov Conf* 2006:489–93.
27. Black I, Chua KL. Laser cutting of thick ceramic tile. *Opt Laser Technol* 1997;**29**(4):193–205.
28. Chung CK, Lin SL. CO_2 laser micromachined crackless through holes of Pyrex 7740 glass. *Int J Mach Tool Manuf* 2010;**50**(11):961–8.
29. Chung CK, Sung YC, Huang GR, Hsiao EJ, Lin WH, Lin SL. Crackless linear through-wafer etching of Pyrex glass using liquid-assisted CO_2 laser processing. *Appl Phys A-Mater* 2009;**94**(4):927–32.
30. Tsai CH, Li CC. Investigation of underwater laser drilling for brittle substrates. *J Mater Process Technol* 2009;**209**(6):2838–46.
31. Auerkari P. Mechanical and physical properties of engineering alumina ceramics. Finland: VTT Manufacturing Technology; 1996.
32. Negarestani R, Sundar M, Sheikh MA, Mativenga P, Li L, Li ZL, et al. Numerical simulation of laser machining of carbon-fibre-reinforced composites. *Proc Inst Mech Eng B-J Eng* 2010;**224**(7):1017–27.
33. Hale GM, Querry MR. Optical constants of water in the 200-nm to 200-μm wavelength region. *Appl Opt* 1973;**12**(3):555–63.
34. Samant AN, Dahotre NB. Laser machining of structural ceramics – a review. *J Eur Ceram Soc* 2009;**29**:969–93.
35. Yang LJ, Wang Y, Tian ZG, Cai N. YAG laser cutting soda-lime glass with controlled fracture and volumetric heat absorption. *Int J Mach Tool Manuf* 2010;**50**(10):849–59.
36. Govindjee S, Kay GJ, Simo JC. Anisotropic modelling and numerical simulation of brittle damage in concrete. *Int J Numer Meth Eng* 1995;**38**(21):3611–33.
37. Wang W, Huang Y, Grujicic M, Chrisey DB. Study of impact-induced mechanical effects in cell direct writing using smooth particle hydrodynamic method. *J Manuf Sci E-Trans ASME* 2008;**130**(2), 021012-1-021012-10.
38. Joseph HA, Paul C, Vladimir A, Thang N. Simulation of die filling in gravity die casting using SPH and MAGMAsoft. In: *Second international conference on CFD in the minerals and process industries*. Melbourne, Australia: CSIRO; 1999. p. 423–8.
39. Monaghan JJ, Gingold RA. Shock simulation by the particle method SPH. *J Comput Phys* 1983;**52**:374–89.
40. Allcock G, Dyer PE, Elliner G, Snelling HV. Experimental observations and analysis of CO_2 laser-induced microcracking of glass. *J Appl Phys* 1995;**78**(12):7295–303.
41. Mueller RE, Bird J, Duley WW. Laser drilling into an absorbing liquid. *J Appl Phys* 1992;**71**(2):551–6.
42. Voisey KT, Kudesia SS, Rodden WSO, Hand DP, Jones JDC, Clyne TW. Melt ejection during laser drilling of metals. *Mater Sci Eng A-Struct* 2003;**356**:414–24.
43. Li L, Achara C. Chemical assisted laser machining for the minimisation of recast and heat affected zone. *CIRP Ann-Manuf Technol* 2004;**53**(1):175–8.
44. Lu YF, Ye KD. Laser-induced etching of polycrystalline Al_2O_3TiC in KOH aqueous solution. *Appl Phys A* 1996;**62**:43–9.
45. Horisawa H, Akimoto N, Ashizawa H, Yasunaga N. Effects of a quartz beam-guide on high-precision laser-assisted etching of Al_2O_3 ceramics. *Surf Coat Technol* 1999;**112**:389–93.
46. Nowak R, Metev S, Sepold G. Nd:YAG-laser-induced wet chemical etching of titanium and stainless steel. *Sens Actuat A-Phys* 1995;**51**:41–5.